12-11-2017

Nonlinear Gravity Wave Forcing as a Source of Acoustic Waves in the Mesosphere, Thermosphere, and Ionosphere

J. B. Snively
Embry-Riddle Aeronautical University, snivelyj@erau.edu

AGU PUBLICATIONS

Geophysical Research Letters

RESEARCH LETTER
10.1002/2017GL075360

Key Points:
- Strong gravity waves (GWs) exhibit nonlinear fluxes of vertical momentum
- Nonlinear GW fluxes may force harmonic acoustic waves (AWs)
- AWs may be detectable above interacting GW fields and overturning regions

Supporting Information:
- Supporting Information S1

Correspondence to:
J. B. Snively,
snivelyj@erau.edu

Citation:
Snively, J. B. (2017). Nonlinear gravity wave forcing as a source of acoustic waves in the mesosphere, thermosphere, and ionosphere. *Geophysical Research Letters*, *44*, 12,020–12,027. https://doi.org/10.1002/2017GL075360

Received 17 AUG 2017
Accepted 30 OCT 2017
Accepted article online 6 NOV 2017
Published online 11 DEC 2017

Nonlinear Gravity Wave Forcing as a Source of Acoustic Waves in the Mesosphere, Thermosphere, and Ionosphere

J. B. Snively[1]

[1]Department of Physical Sciences, Embry-Riddle Aeronautical University, Daytona Beach, FL, USA

Abstract Numerical simulations demonstrate theoretical predictions that gravity waves with short periods (~4–8 min) in the mesosphere and lower thermosphere may force secondary acoustic waves, with harmonic periods (~2-4 minutes), that can reach detectable amplitudes in the thermosphere and ionosphere. The mechanism is through their vertical fluxes of vertical momentum, which lead to forcing as they are disrupted by varying stratification or instability. This is shown likely to occur where horizontally or radially opposing gravity waves interact at large amplitudes, such as above large convective sources, and after overturning. Evanescence and reflection of the waves can lead to further enhancements of the vertical fluxes and the potential for forcing. Results thus identify one of likely several mechanisms for the nonlinear conversion from gravity waves to acoustic waves, to elucidate an unappreciated source of vertical coupling.

1. Introduction

Acoustic waves (AWs) in the ionosphere, thermosphere, and mesosphere (ITM) above convection, while observed for decades (e.g., Georges, 1973), have recently received new attention as their perturbations can be mapped in Global Positioning System (GPS) total electron content (TEC) data (e.g., Nishioka et al., 2013). The AWs in data, with periods ~1–4 min, are often accompanied by detectable gravity waves (GWs) at greater radii (e.g., Lay et al., 2015), typically with periods of ~6–30 min. Both AWs and GWs, such as reported by Nishioka et al. (2013), are often observed to persist over long periods of time (hours), likely due to reflection and ducting in addition to the persistence of forcing.

Tropospheric convective disturbances may impose thermal and mechanical forcing over short periods, leading to the generation of upward propagating AWs and GWs (e.g., Walterscheid et al., 2003; Vadas, 2013). These waves may become trapped below the lower thermosphere, thus forming resonances or ducted modes, while gradually leaking upward into the thermosphere-ionosphere. This provides a simple explanation for their observed persistence following seismic events and severe weather (e.g., Matsumura et al., 2012; Nishioka et al., 2013, and references therein). Modeled "updraft" sources, used to demonstrate primary AW and GW observability in the mesospheric hydroxyl airglow by Snively (2013) and ionospheric TEC by Zettergren and Snively (2013), also excite resonant AWs and GWs similar to those reported in thermospheric observations. In addition to filtering via reflection and resonance, the spectral coherence of AWs is enhanced by viscous dissipation and the vertical integration of TEC measurements, which typically limits the observable bandpass to periods longer than 1 min (Zettergren & Snively, 2015).

Model simulations of Zettergren et al. (2017) support that reflection and resonance processes enhance persistence of AW signatures, especially above larger (more directive) source regions. Indeed, observations reveal correlations between AW occurrences and larger source spatial scales (Lay et al., 2015). Shao and Lay (2016) also found that AWs correlate with convective downdrafts and stratiform regions that may be offset from the most active convection. This also suggests correlation with electric discharge events in the troposphere and above (e.g., Pasko, 2009; de Larquier & Pasko, 2010), although it is unclear whether these fast processes couple well to the ~1–4 min period AWs detected.

Here a simple nonlinear mechanism is demonstrated for the generation of acoustic waves, which may be either transient or persistent, via nonlinearity of gravity waves especially as they interact or overturn. By this mechanism, AWs are generated with periods ~2–4 min, consistent with harmonics of GWs with periods of ~4–8 min (or longer, when GWs break/cascade to smaller scales and shorter periods while retaining sufficient coherence). The mathematical and physical basis for these investigations is well established from

aeroacoustics (e.g., Lighthill, 1952; Colonius & Lele, 2004). Results are interpreted through the nonlinear advective flux term of the momentum equation (corresponding with Lighthill's (1952) simplified effective stress tensor $\tau \simeq \rho\mathbf{vv}$) and its divergences interpreted as a source of acceleration ("body forces"), that is, $\mathbf{F} = -\nabla \cdot (\rho\mathbf{vv})$. Under certain conditions that will be demonstrated, wave vertical fluxes of vertical momentum ($= \rho w^2$), when averaged over a horizontal wavelength, reveal the possibilities for vertical forcing that may be periodic at the GW's second harmonic. As nonlinear GW fluxes are disrupted by varying stratification or instability, radiation of AWs may occur.

Harmonic generation of secondary gravity waves, via nonlinearity of fluxes, has also been demonstrated theoretically, for primary GWs passing through ducts that may subsequently capture their harmonics (Chimonas et al., 1996), and numerically, in the vicinity of GW breaking regions (Franke & Robinson, 1999) and where secondary ducted GWs may be excited by finite-amplitude primary GW in the mesosphere and thermosphere (Snively and Pasko, 2003, 2008). These processes have also been identified in an oceanic context (Sutherland, 2016, and references cited therein). The mechanism reported here is related to the same interaction processes (which lead to harmonic secondary GWs) and also elucidates a pathway for acoustic-gravity wave coupling and conversion from GWs to AWs that are able to propagate deeply into the ITM (e.g., Walterscheid & Hecht, 2003).

The spatial structure and temporal evolution of fluxes is visualized first via a "toy" analytical model in section 2, to identify the specific scenarios under which interactions can lead to harmonic vertical forcing. In section 3, 2-D and 3-D nonlinear numerical models are used to simulate GWs as they interfere and interact, and approach instability and overturning. Scenarios are considered in a horizontally periodic domain to elucidate forcing mechanism and quantify the resulting AW fields. Four simulations are performed, for cases where a controlled fraction of the GW spectrum may be subject to conversion: (I) a right-going and upward propagating GW packet in 2-D; (II and II-Weak) opposing/interfering left- and right-going upward propagating GW packets in 2-D, at moderate and weak amplitudes (to confirm quadratic sensitivity of AW responses to GW amplitude); and (III) a right-going and upward propagating GW packet in 3-D to demonstrate robustness of the mechanism. Discussion and Conclusions are summarized in section 4.

2. Analytical Toy Model Results

The role of the vertical flux of vertical momentum, quantified here from the square of vertical velocity w^2, is first demonstrated graphically for short period GWs using a toy analytical model. Simple GW solutions of the form $w(x,z,t) = W\cos(\omega t - kx - mz)$ are specified in an isothermal atmosphere (surface density $\rho_o =$ 1.2 kg/m^3 and pressure $p_o = 1 \times 10^5$ Pa, where acceleration of gravity $g = 9.8$ m/s^2, ratio of specific heats $\gamma = c_p/c_v = 1.4$, speed of sound $c_s = \sqrt{\gamma p/\rho} = 341$ m/s, scale height $H = c_s^2/(\gamma g) = 8.5$ km, Brunt-Väisälä frequency $N = \sqrt{(1-1/\gamma)g/H} = 0.0181$ rad/s, and acoustic cutoff frequency $\omega_a = \sqrt{c_s^2/(4H^2)} = 0.0201$ rad/s). Gravity waves (Figure 1a) are specified as right going and upgoing (w_1 with $m < 0, k > 0$) and left going and downgoing (w_3 with $m > 0, k < 0$) and (Figure 1b) right going and downgoing (w_1 with $m > 0, k > 0$) and left going and upgoing (w_4 with $m < 0, k < 0$).

Superpositions of GW velocity fields are shown in Figure 1c. Arrows indicate phase and group progression for two cases: Right-upgoing (w_1) and right-downgoing (w_2) waves, such as following reflection, yield a vertically standing wave with rightward phase progression. Right-upgoing w_1 and left-upgoing w_4 waves, such as may be present above horizontally (or radially) extended convective sources, yields a GW superposition with upward group and downward phase velocity. This is a Cartesian analog to the diffractively focused cylindrical waves above thunderstorms, investigated by Pasko et al. (1997), where waves were radially axisymmetric about the z axis and upward propagating.

The fluxes of the superposed GWs are interpreted as follows: Figure 1d shows that ducting or reflecting GWs carry layered vertical fluxes of vertical momentum, which do not vary in time; Figure 1e shows that horizontally opposed interfering GWs carry vertical fluxes of vertical momentum that vary at the second harmonic period, while progressing downward; Figure 1f shows that horizontally opposed interfering GWs, while also reflecting, exhibit quasiperiodic, vertically stationary fluxes at the GW second harmonic period. This scenario suggests strong potential for forcing as interfering waves reflect together as they approach evanescence (e.g., Walterscheid & Hecht, 2003), where their vertical fluxes of vertical momentum are also maximized.

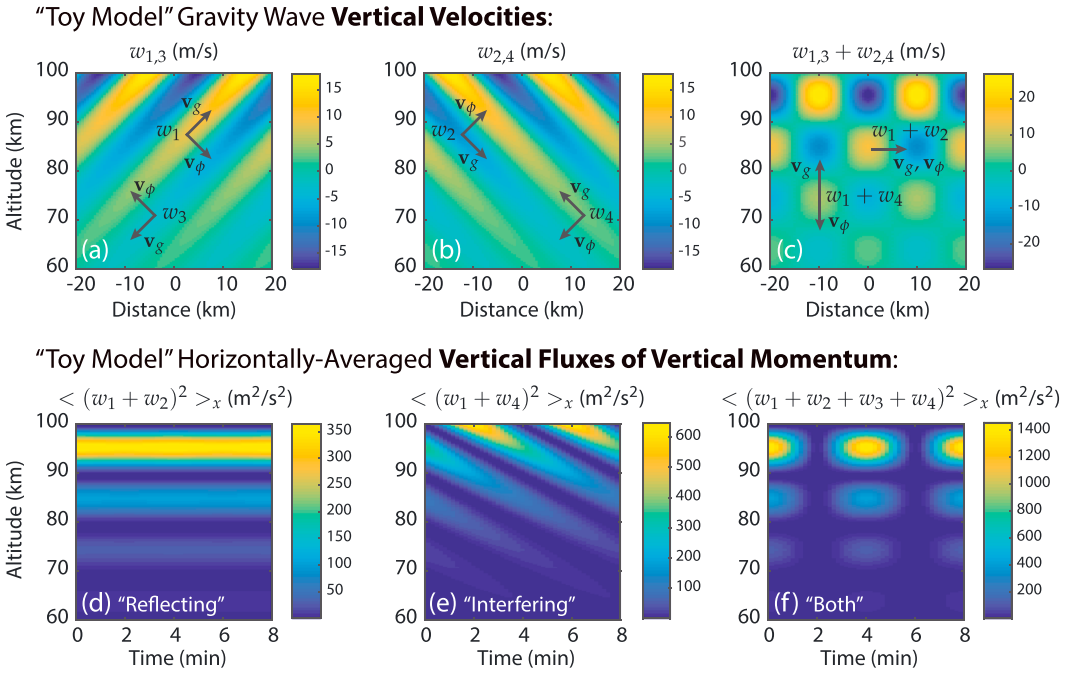

Figure 1. Toy model vertical velocities (a) w_1 or w_3 for right-upgoing or left-downgoing waves and (b) w_2 or w_4 for left-upgoing or right-downgoing waves, and (c) the superposed velocity fields, with phase progression indicated. Time evolutions of horizontally averaged flux terms w^2 for superpositions of (d) up and down right-going waves, (e) left- and right-upgoing waves, and (f) all four waves superposed.

In summary, Figures 1d–1f demonstrate that the "interfering" waves (especially those also subject to reflection) exhibit fluxes that can contribute to harmonic vertical forcing. Numerically, in the next section, we will demonstrate that disruption of these fluxes, such as by varying stratification and evanescence, leads to radiation of acoustic waves and that overturning instability can further contribute. These cases are idealized, but it is reasonable to assume that interactions of this form are common. Indeed, gravity waves are routinely observed above large convective systems (e.g., Miller et al., 2015, and references cited therein), and short period GWs in particular will be subject to interactions (and instabilities at finite amplitudes) as they are focused above extended source regions (Pasko et al., 1997).

3. Numerical Model Results

The numerical model used is that of Snively and Pasko (2008), in its updated form described by Zettergren and Snively (2015), here applied in 2-D and 3-D Cartesian domains. It is a solution to the nonlinear, compressible, Navier-Stokes equations in a realistic atmosphere via a finite volume method (Bale et al., 2002; LeVeque, 2002) implemented in a modified version of Clawpack 4.2 (e.g., Clawpack Development Team, 2002). For this investigation, it functions as an implicit large-eddy simulation, although physical viscosity where waves primarily break (above ~100 km altitude) exceeds numerical dissipation.

The mechanisms, demonstrated numerically, occur robustly over a wide range of conditions; nevertheless, their specific evolutions are sensitive to the ambient atmosphere, here specified via NRLMSISE-00 (Hedin, 1991; Picone et al., 2002). The profiles are chosen (arbitrarily) for 12:00 UT (~23:20 LST), 14 July 2014, −45° latitude, 170° longitude. For all case studies (I, II, II-Weak, and III), the domain is horizontally periodic, reflective at bottom (Earth's surface) and open at top. Horizontal and vertical domains are 160 by 1,280 grid points, with uniform vertical and horizontal cell dimensions of $\Delta x = \Delta z = 125$ m, that is, 20 by 160 km. For Case III, the 3-D domain is extended 10 km in the transverse (y) direction.

The sources for all cases are sinusoidal vertical accelerations with Gaussian envelopes in time and altitude, centered about the bottom boundary. Their forcing functions are given by $\mathcal{F}_z = A(x,t)\exp\left(-\frac{(t-t_0)^2}{2\sigma_t^2} - \frac{z^2}{2\sigma_z^2}\right)$.

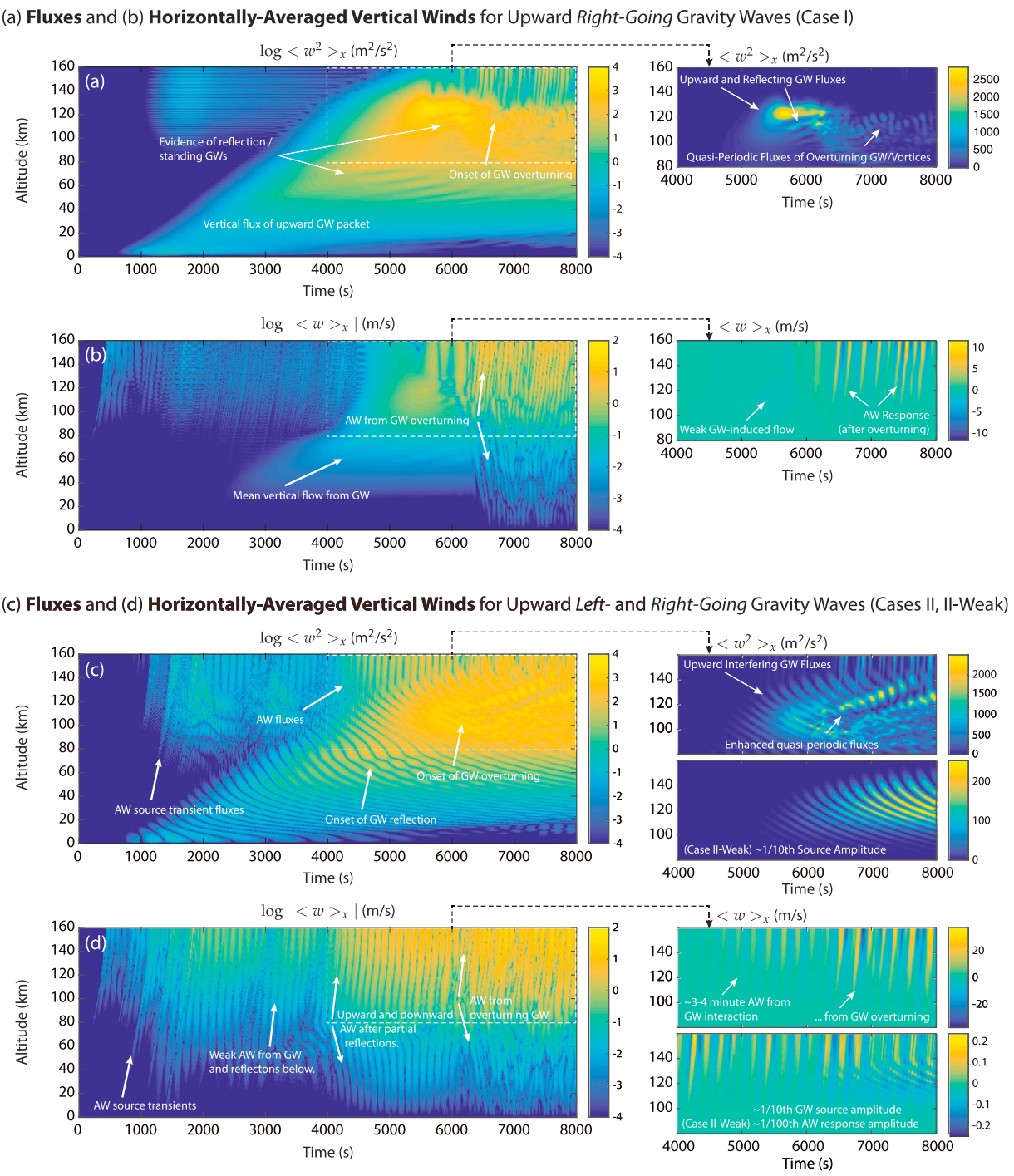

Figure 2. Time evolutions of horizontally averaged (a, c) vertical fluxes and (b, d) wind magnitudes for Case I (right-going) and Case II (left- and right-going) gravity waves, plotted on log scales, with subpanels (on right side) showing isolated data plotted on linear scales. Subpanels are included for Case II-Weak (for one tenth source amplitude of Case II), revealing the quadratic amplitude relationship between primary GWs and secondary AWs.

The sinusoids for Cases I and III have traveling waveform $A(x,t) = A_o \sin(\omega(t-t_o)-kx)$, while Case II uses standing wave oscillators of the form $A(x,t) = A_o \sin(\omega(t-t_o)) \cdot \sin(kx)$. Sources for Cases I and II are specified with common parameters $A_o = 0.03$ m/s^2 ($A_o = 0.003$ m/s^2 for Case II-Weak), $\omega = 0.01047$ rad/s, $k_x = \pi \times 10^-4$ rad/m, $\sigma_z = 2 \times 10^3$ km, $\sigma_t = 255$ s, and $t_o = 1.275 \times 10^3$ s. Case III differs, with $A = 0.04$ m/s^2, $\omega = 0.012831$ rad/s, $\sigma_t = 208$ s, and $t_o = 1 \times 10^3$ s, to reduce simulation time; nevertheless, the leading ~5–8 min period GWs break first in both Cases I and III, so that their resulting nonlinear evolutions are similar.

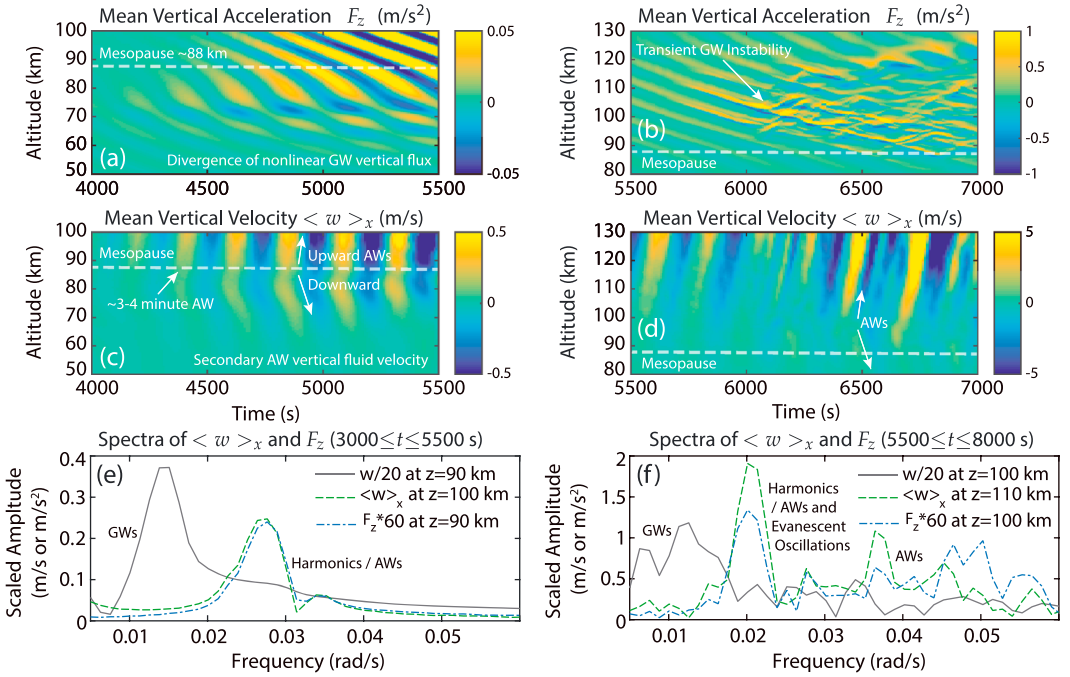

Figure 3. Case II evolutions are shown for two altitude ranges and spans of time, showing emergence of AWs before overturning ($50 \le z \le 100$ km and $4{,}000 \le t \le 5{,}500$ s) and after ($80 \le z \le 130$ km and $5{,}500 \le t \le 7{,}000$ s). (a, b) Divergences of horizontally averaged vertical fluxes of vertical momentum, indicating potential for forcing and acceleration. (c, d) Horizontally averaged vertical winds. (e and f) Spectra for vertical velocities at fixed positions (solid line; to reveal GWs), horizontally averaged accelerations (dash-dotted line; to reveal forcing), and horizontally averaged vertical velocity (dashed line; to reveal AWs) at heights 10 km above.

Figure 2a shows the time evolutions of vertical momentum flux (horizontally averaged, excluding factor of density) for Case I, plotted on $\log_{10}$ and linear scales. The GW propagates upward and, after 4,000 s (<80 km), exhibits partial reflection (leading to apparent layering of fluxes). The GWs continue upward and after ~6,000 s begin to overturn. Resulting quasiperiodic fluxes evolve near 100–120 km, simultaneous to forcing of AWs that are revealed clearly in Figure 2b, showing horizontally averaged vertical fluid velocities reaching ±10 m/s in the lower thermosphere. Figure 2c shows the vertical momentum flux, plotted similarly, for Case II. The fluxes clearly show harmonics, due to cancelation of fluxes of horizontal momentum as GWs propagate both to the left and right (e.g., interfering horizontally standing waves). They have no net impact on horizontal flow and, instead, impose vertical harmonic forcing. Figure 2d shows the horizontally averaged vertical fluid velocity, with radiation of acoustic waves upward and downward (indicated by steep phase lines, with upward phase velocity and upward group velocity) as the waves partially reflect across mesopause ($4{,}000 < t < 6{,}000$ s) and, later, after overturning (>6,000 s). These secondary AW amplitudes exceed ±30 m/s in the lower thermosphere, which may be readily detectable in ionospheric data (Zettergren & Snively, 2015).

Figures 2c and 2d show subplots for Case II-Weak, where GW source amplitude is reduced by a factor 1/10 as compared to Case II. The resulting AW amplitudes are reduced by a factor of ~1/100, confirming their quadratic sensitivity to the primary GW amplitude and, thus, their nonlinear origin—that is, the amplitude of secondary AWs scales quadratically, rather than linearly, with the amplitude of the primary GWs.

Figures 3a and 3b quantify the time evolution of the divergence of horizontally averaged vertical flux of vertical momentum, which is consistent with an acceleration (in the momentum conservation equation) when not balanced by a pressure gradient force. This is shown together with horizontally averaged vertical velocity in Figures 3c and 3d, which reveals the presence of AWs. Figures 3a and 3c (showing 4,000 to 5,500 s and 50 to 100 km altitude) thus reveal GW harmonics and AW responses, respectively, prior to breaking, about the mesopause stability minimum where they are partially reflected. Spectra (for 3,000 to 5,500 s) in Figure 3e of GWs and mean vertical flux divergences at 90 km, and resulting mean vertical AW winds at 100 km, reveal clear harmonic relationships. Likewise, in Figures 3b and 3d (showing 5,500 to 7,000 s and 80 to 130 km altitude),

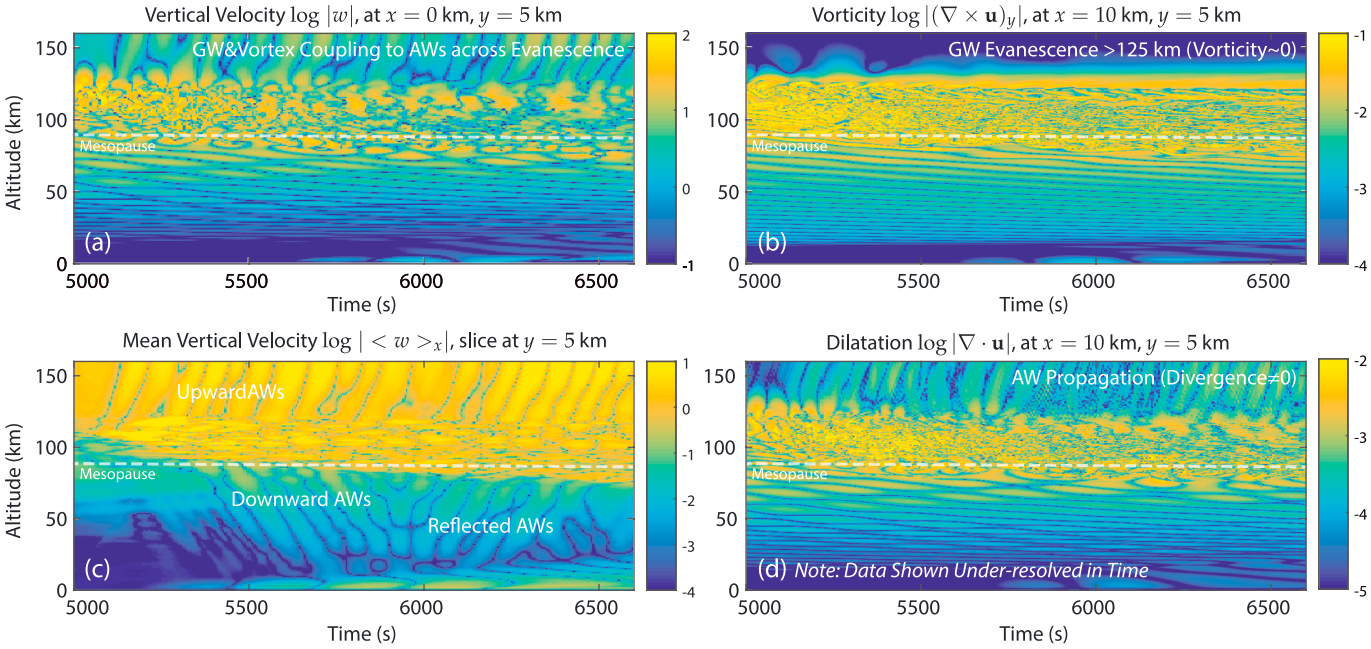

Figure 4. Case III (3D) evolutions, during overturning, are shown for log-scale absolute vertical velocity measured (a) along a column and (c) horizontally-averaged across the domain, and for (b) absolute *y*-vorticity and (d) absolute dilatation fields each measured along a central column.

the flux divergence (acceleration) field after onset of overturning reveals forcing at AW timescales, which correlates with the generation of harmonic and broadband AWs with periods of minutes at moderate amplitudes. These are clearly revealed in Figure 3f, showing spectra for 5,500 to 8,000 s, with greater complexity due to instability and additional harmonics.

Figure 4 shows results of Case III, confirming the process in 3-D, yielding AW responses very similar to Case I. Note that the wind shear and instability following GW self-acceleration (e.g., Fritts et al., 2015 and references therein) commenced at earlier times, not shown here, and were confined primarily to the lower thermosphere; what remains is a layer where GWs continue to break in the resulting flow. Log-scale absolute vertical velocity, along a single column (Figure 4a), reveals the presence of AWs at altitudes above where GWs become evanescent above their breaking layer. The AW field is more clearly shown in horizontally averaged vertical velocity (Figure 4c), where both upward and downward propagating AWs are emitted about the layer. Figures 4b and 4d, respectively, show the time evolutions of absolute values of *y* vorticity (*y* component of curl) and dilatation (divergence), each measured along a column in the center of the domain. The vorticity reveals continued incompressible features of GW disturbances and overturning above mesopause; the GW becomes evanescent above (see the absence of vortical perturbations >125 km). The dilatation (Figure 4d) reveals compressional features and, in particular, AWs in the lower thermosphere, where the GW disturbances become evanescent.

The demonstrated nonlinear mechanism is most effective where interfering finite-amplitude GWs approach evanescence and reflection, and where they begin to overturn with reduced tendencies toward shear instability. In both scenarios, vertical fluxes of vertical momentum may be large and acoustic-gravity wave coupling more effective (e.g., Walterscheid & Hecht, 2003). For simplicity, to demonstrate the primary effects of interest within the nonlinear models, initial (ambient) winds have been excluded. Nevertheless, results may be affected by winds that Doppler shift, filter, and/or displace the wave field above a strong convective source. Although not depicted, strong shear following self-acceleration does occur in Cases I and III, where right-going GWs are specified, leading to a wind jet >100 m/s above mesopause (e.g., Fritts et al., 2015). For Case II, the interfering left- and right-going primary GWs preclude self-acceleration—and tendency toward shear instability—as fluxes of horizontal momentum cancel and vertical fluxes are enhanced; thus, the GWs attain larger amplitudes and generate stronger AWs.

4. Discussion and Conclusions

The acoustic waves presented here are forced primarily through disruptions of nonlinear gravity wave vertical fluxes of vertical momentum. Consistent with this relationship, the secondary AWs have frequencies that relate harmonically and amplitudes that depend quadratically with their primary GWs. The mechanism was found most effective when horizontally opposed GWs interfered and reached instability at large amplitudes (approximately tens of m/s). Dispersion of GWs ensures that the spectrum of waves above a convective source is close to the Brunt-Väisälä period and thus able to force harmonics at AW periods. Indeed, the existence of concentric short-period GW structures in airglow that extends from zero radius (e.g., Sentman et al., 2003; Vadas et al., 2012) provides evidence for focusing and interference of radially opposed GWs above their sources, as predicted by Pasko et al. (1997), which may create regions favorable for coupling from nonlinear GWs to secondary AWs. Interacting or overturning GW may couple with AWs most effectively through layers where GW becomes evanescent (e.g., Walterscheid & Hecht, 2003), near where vertical fluxes are also maximized. This process may be most effective across thin layers, such as mesopause, where the effective accelerations may occur over a region shallower than an acoustic half-wavelength. The mechanism also occurs, over a broader spectrum, during instability leading to GW breaking and evolving vortices, with or without self-acceleration (e.g., Fritts et al., 2015) as the specific forcing mechanism is a result of GW-induced vertical forcing rather than horizontal forcing.

Recent observations of persistent AWs may be well explained by linear resonance and ducting above sources with time scales short enough to generate both AWs and GWs directly (spectral content above the Brunt-Väisälä frequency) (Nishioka et al., 2013). The proposed nonlinear mechanism provides a complementary explanation, perhaps relevant to findings of Lay et al. (2015) and Shao and Lay (2016): (1) It is likely effective above large storms that generate strong, widespread GW fields, and (2) due to GW dispersion, it may occur in regions offset from the most active convection. Notably, the amplitudes of secondary AWs reported here are similar to the directly forced AWs reported by Snively (2013) in the thermosphere (approximately tens of m/s) and are thus readily detectable in GPS TEC (e.g., Zettergren & Snively, 2013). In test cases, not shown, AW generation was also found to occur for GW interactions or breaking in the stratosphere; this enables greater amplification of AWs as they must propagate upward through more density scale heights before reaching the ITM. Further investigations are necessary to discern and assess the relative contributions of primary and secondary AW forcing mechanisms, including occurrence rates and resulting spectra and amplitudes.

Other physical processes are anticipated to be important as well, such as during transient GW breaking events (discussed in communications with D. C. Fritts and B. Laughman in June 2017, regarding AWs in their 3-D simulations of mountain GWs; AWs were also identified, but neither analyzed nor reported, in the 2-D simulations of Heale et al., 2017). The sensitivity to model resolution and numerics must be investigated carefully for scenarios involving rapid cascades of GWs to very small scales. AWs generated by *nonbreaking* GW, however, are forced over spatial scales larger than the primary GWs; Case II results before ~5,500 s are not sensitive to resolution but may depend on GW packet scales. Results from aeroacoustics can provide guidance into the broad range of atmospheric dynamics (e.g., waves, instabilities, and turbulence) that may lead to AW radiation (e.g., Colonius & Lele, 2004, and references therein). Recent measurements also suggest opportunities for experimental investigations of atmospheric generation of AWs at higher (still infrasonic) frequencies (Bowman & Lees, 2015).

The mechanism shown here enables generation of AWs that may occur persistently as strong GWs evolve nonlinearly above sources or transiently following rapid GW breakdown. As proposed by Hickey et al. (2001) and Walterscheid and Hickey (2005), continuous forcing of AWs by various sources may contribute to thermospheric heating, a process that remains to be quantified. More recently, on this basis, heating by upward propagating AW and GW has been proposed to explain high thermospheric temperatures above Jupiter's Great Red Spot (O'Donoghue et al., 2016). The observability and potential importance of AWs in the Earth's thermosphere—and their primary and secondary generation mechanisms—may be investigated via new modeling and data (e.g., airglow imaging and ionospheric TEC) where AWs and GWs can be simultaneously diagnosed.

Acknowledgments
Research was supported under NSF CAREER Award AGS-1151746 to Embry-Riddle Aeronautical University. J. B. Snively acknowledges encouraging discussions with D. C. Fritts, B. Laughman, and C. J. Heale at the 2017 NSF CEDAR Workshop, regarding their complementary identifications of acoustic waves in 2-D and 3-D mountain wave breaking simulations. Also gratefully acknowledged are the helpful comments of two anonymous reviewers. Model simulation data shown in figures are included as ASCII text files in a .zip archive as supporting information and are available in other formats upon request.

References

Bale, D. S., LeVeque, R. J., Mitran, S., & Rossmanith, J. A. (2002). A wave propagation method for conservation laws and balance laws with spatially-varying flux functions. *SIAM Journal of Scientific Computing*, *24*, 955–978.

Bowman, D. C., & Lees, J. M. (2015). Infrasound in the middle stratosphere measured with a free-flying acoustic array. *Geophysical Research Letters*, *42*, 10,010–10,017. https://doi.org/10.1002/2015GL066570

Chimonas, G. H., Hauser, H. M., & Bennett, R. D. (1996). The excitation of ducted modes by passing internal waves. *Physics of Fluids*, *8*(6), 1486–1505.
Clawpack Development Team (2002). Clawpack software version 4.2. Retrieved from http://www.clawpack.org
Colonius, T., & Lele, S. K. (2004). Computational aeroacoustics: Progress on nonlinear problems of sound generation. *Progress in Aerospace Sciences*, *40*, 345–416. https://doi.org/10.1016/j.paerosci.2004.09.001
de Larquier, S., & Pasko, V. P. (2010). Mechanism of inverted-chirp infrasonic radiation from sprites. *Geophysica Research Letters*, *37*, L24803. https://doi.org/10.1029/2010GL045304
Franke, P. M., & Robinson, W. A. (1999). Nonlinear behavior in the propagation of atmospheric gravity waves. *Journal of the Atmospheric Sciences*, *56*, 3010–3027.
Fritts, D. C., Laughman, B., Lund, T. S., & Snively, J. B. (2015). Self-acceleration and instability of gravity wave packets: 1. Effects of temporal localization. *Journal of Geophysical Research: Atmospheres*, *120*, 8783–8803. https://doi.org/10.1002/2015JD023363
Georges, T. M. (1973). Infrasound from convective storms: Examining the evidence. *Reviews of Geophysics and Space Physics*, *11*(3), 571–594.
Heale, C. J., Bossert, K., Snively, J. B., Fritts, D. C., Pautet, P.-D., & Taylor, M. J. (2017). Numerical modeling of a multiscale gravity wave event and its airglow signatures over Mount Cook, New Zealand, during the DEEPWAVE campaign. *Journal of Geophysical Research: Atmospheres*, *122*, 846–860. https://doi.org/10.1002/2016JD025700
Hedin, A. E. (1991). Extension of the MSIS thermospheric model into the middle and lower atmosphere. *Journal of Geophysical Research*, *96*(A2), 1159–1172.
Hickey, M. P., Schubert, G., & Walterscheid, R. L. (2001). Acoustic wave heating of the thermosphere. *Journal of Geophysical Research*, *106*(A10), 21,543–21,548.
Lay, E. H., Shao, X.-M., Kendrick, A. K., & Carrano, C. S. (2015). Ionospheric acoustic and gravity waves associated with midlatitude thunderstorms. *Journal of Geophysical Research: Space Physics*, *120*, 6010–6020. https://doi.org/10.1002/2015JA021334
LeVeque, R. J. (2002). *Finite volume methods for hyperbolic problems*. Cambridge, UK: Cambridge University Press.
Lighthill, M. J. (1952). On sound generated aerodynamically: I. General theory. *Proceedings of the Royal Society A*, *211*(1107), 564–587. https://doi.org/10.1098/rspa.1952.0060
Matsumura, M., Shinagawa, H., & Iyemori, T. (2012). Horizontal extension of acoustic resonance between the ground and the lower thermosphere. *Journal of Atmospheric and Solar-Terrestrial Physics*, *75–76*, 127–132. https://doi.org/10.1016/j.jastp.2011.12.003
Miller, S. D., Straka III, W. C., Yue, J., Smith, S. M., Alexander, M. J., Hoffman, L., … Partain, P. T. (2015). Upper atmospheric gravity wave details revealed in nightglow satellite imagery. *Proceedings of the National Academy of Sciences of the United States of America*, *112*(49), E6728–E6735. https://doi.org/10.1073/pnas.1508084112
Nishioka, M., Tsugawa, T., Kubota, M., & Ishii, M. (2013). Concentric waves and short-period oscillations observed in the ionosphere after the 2013 Moore EF5 tornado. *Geophysical Research Letters*, *40*, 5581–5586. https://doi.org/10.1002/2013GL057963
O'Donoghue, J., Moore, L., Stallard, T. S., & Melin, H. (2016). Heating of Jupiter's upper atmosphere above the Great Red Spot. *Nature*, *536*, 190–192. https://doi.org/10.1038/nature18940
Pasko, V. P. (2009). Mechanism of lightning-associated infrasonic pulses from thunderclouds. *Journal of Geophysical Research*, *114*, D08205. https://doi.org/10.1029/2008JD011145
Pasko, V. P., Inan, U. S., & Bell, T. F. (1997). Sprites as evidence of vertical gravity wave structures above mesoscale thunderstorms. *Geophysical Research Letters*, *24*(14), 1735–1738.
Picone, J. M., Hedin, A. E., Drob, D. P., & Aikin, A. C. (2002). NRLMSISE-00 empirical model of the atmosphere: Statistical comparisons and scientific issues. *Journal of Geophysical Research*, *107*(A12), 1468. https://doi.org/10.1029/2002JA009430
Sentman, D. D., Wescott, E. M., Picard, R. H., Winick, J. R., Stenbaek-Nielsen, H. C., Dewan, E. M., … Morrill, J. (2003). Simultaneous observations of mesospheric gravity waves and sprites generated by a midwestern thunderstorm. *Journal of Atmospheric and Solar-Terrestrial Physics*, *65*, 537–550.
Shao, X.-M., & Lay, E. H. (2016). The origin of infrasonic ionosphere oscillations over tropospheric thunderstorms. *Journal of Geophysical Research: Space Physics*, *121*, 6783–6798. https://doi.org/10.1002/2015JA022118
Snively, J. B. (2013). Mesospheric hydroxyl airglow signatures of acoustic and gravity waves generated by transient tropospheric forcing. *Geochemistry, Geophysics, Geosystems*, *40*, 4533–4537. https://doi.org/10.1002/grl.50886
Snively, J. B., & Pasko, V. P. (2003). Breaking of thunderstorm-generated gravity waves as a source of short-period ducted waves at mesopause altitudes. *Geophysical Research Letters*, *30*(24), 2254. https://doi.org/10.1029/2003GL018436
Snively, J. B., & Pasko, V. P. (2008). Excitation of ducted gravity waves in the lower thermosphere by tropospheric sources. *Journal of Geophysical Research*, *113*, A06303. https://doi.org/10.1029/2007JA012693
Sutherland, B. R. (2016). Excitation of superharmonics by internal modes in non-uniformly stratified fluids. *Journal of Fluid Mechanics*, *793*, 335–352. https://doi.org/10.1017/jfm.2016.108
Vadas, S. L. (2013). Compressible f-plane solutions to body forces, heatings, and coolings, and application to the primary and secondary gravity waves generated by a deep convective plume. *Journal of Geophysical Research: Space Physics*, *118*, 2377–2397. https://doi.org/10.1002/jgra.50163
Vadas, S. L., Yue, J., & Nakamura, T. (2012). Mesospheric concentric gravity waves generated by multiple convective storms over the North American Great Plain. *Journal of Geophysical Research*, *117*, D07113. https://doi.org/10.1029/2011JD017025
Walterscheid, R. L., & Hecht, J. H. (2003). A reexamination of evanescent acoustic-gravity waves: Special properties and aeronomical significance. *Journal of Geophysical Research*, *108*(D11), 4340. https://doi.org/10.1029/2002JD002421
Walterscheid, R. L., & Hickey, M. P. (2005). Acoustic waves generated by gusty flow over hilly terrain. *Journal of Geophysical Research*, *110*, A10307. https://doi.org/10.1029/2005JA011166
Walterscheid, R. L., Schubert, G., & Brinkman, D. G. (2003). Acoustic waves in the upper mesosphere and lower thermosphere generated by deep tropical convection. *Journal of Geophysical Research*, *108*(A11), 1392. https://doi.org/10.1029/2003JA010065
Zettergren, M. D., & Snively, J. B. (2013). Ionospheric signatures of acoustic waves generated by transient tropospheric forcing. *Geophysical Research Letters*, *40*, 5345–5349. https://doi.org/10.1002/2013GL058018
Zettergren, M. D., & Snively, J. B. (2015). Ionospheric response to infrasonic-acoustic waves generated by natural hazard events. *Journal of Geophysical Research: Space Physics*, *120*, 8002–8024. https://doi.org/10.1002/2015JA021116
Zettergren, M. D., Snively, J. B., Komjathy, A., & Verkhoglyadova, O. P. (2017). Nonlinear ionospheric responses to large-amplitude infrasonic-acoustic waves generated by undersea earthquakes. *Journal of Geophysical Research*, *122*, 2272–2291. https://doi.org/10.1002/2016JA023159